Chapter 2

Overview of the Observational Data, Analysis Techniques and Numerical Methodology

In this chapter, we describe an overview of various space-borne observatories (e.g., Interface Region Imaging Spectrograph (IRIS), Solar Dynamics Observatory (SDO)), and their onboard instruments (e.g., IRIS Slit-jaw Imager (SJI) and Spectrograph, Atmospheric Imaging Assembly (AIA)), whose data we utilize to derive the scientific results presented in this thesis. We also discuss some data calibration and analysis techniques (for example, image calibration and processing, spectral analysis, Differential Emission Measure (DEM)). The thesis in major is based on MHD modeling of various physical aspects of the cool spicule-like jets. Therefore, we describe the numerical simulation techniques used in the modeling of the solar cool jets, and associated waves, oscillation, shocks, and plasma flows. At the end of this chapter, we briefly discuss the wavelet analysis technique.

The present thesis describes some new scientific results about the cool spicule-like jets and associated plasma processes (e.g., waves, oscillations, shocks, instability, etc) using numerical simulation as well as observations taken from the space-borne instruments. The complementary imaging and spectroscopic observation are used in this thesis in Chapter 5 & 7, which are recorded from the space-borne observatories such as Interface Region Imaging Spectrograph (IRIS) (De Pontieu et al., 2014b) and Solar Dynamics Observatory (SDO) (Pesnell et al., 2012). The physical information is derived from the observations by analysing them using a variety of analysis techniques and procedures, some observational results are utilized to initialize the MHD models. The brief introduction of the observational instruments, data, and analysis tools are provided in this chapter. The simulation of the cool chromospheric jets are performed using PLUTO MHD simulation code (Mignone et al., 2007a). Therefore, we also discuss the details of MHD simulations in this Chapter. Section 2.2 delineate information on various instruments and their observational capabilities. In Section 2.3, the various methodologies associated with different observational data analysis techniques are described. The MHD numerical tools and methodology, which are used in the numerical simulation presented in various forthcoming chapters, are briefly outlined in the Section 2.4. In the Section 2.5, we describe the wavelet analysis technique used in Chapter 3 of the present thesis.

2.1 Observational Perspectives of the Solar Atmosphere

The various layers of the solar atmosphere emits a board range of spectral lines. The multi-wavelength imaging and spectroscopic observations provide an unique tool to study the plasma dynamics and characteristics of various layers of the atmosphere of the Sun (e.g., Curdt et al., 2001; Del Zanna and Mason, 2018; Hinode Review Team et al., 2019; Wilhelm et al., 2007, and references cited therein). Additionally, emissions observed in EUV, soft and hard X-ray, can be used to study the high energy counterparts of various

dynamical plasma processes (e.g., solar jets, flares, magnetic reconnection, etc), which take place in the magnetized and structured atmosphere of the Sun (e.g., Raouafi et al., 2016b; Shibata and Magara, 2011, and references cited therein). The EUV and X-ray emissions provide the diagnostics of a variety of the physical processes that may responsible for the localized coronal heating and mass transport. Most of the UV/EUV emissions infer the formation temperature of the various ions ranging from 10,000 K to 20 MK (Wilhelm et al., 2004). The different spectral lines formed at their specific formation temperature, reveal the specific characterization of the different layer of the Sun's atmosphere. Therefore, we can understand about the various physical plasma processes and significant role of the complex structuring of the magnetic field therein (e.g., Aschwanden, 2019). In addition, since UV/EUV and X-ray emissions are completely absorbed by the Earth's atmosphere, consequently we can not fully understand about the physical processes under the light of such radiations using ground-based instruments. So, we require only the space-based instruments for the analysis of the physical processes seen in UV/EUV, X-rays from the atmosphere of the Sun (e.g., Brosius et al., 1996; Culhane et al., 2007; Wilhelm et al., 2004, and references cited therein). The radiations are generated from the solar atmosphere either by the transition within atoms or molecules. It depends on the temperature range of the specific region of the solar atmosphere. The lower solar atmosphere (e.g., photoshere and chromosphere) contains the ions, electrons, and neutrals due to its lower temperature, while the solar corona mainly consists of highly ionized species/elements. As a results, the continuum emissions take place from the cooler regions of the solar atmosphere (i.e., between photosphere and lower chromosphere), while the emission lines are mostly emitted from the hot corona. Apart from these lines, the solar atmosphere possess the complex magnetic field, which can be measured in terms of its magnitude and polarity using magnetogram and spectro-polerimeteric observations. These observations and estimations of the magnetic field is possible by the radiations emitted in form of magnetically sensitive

spectral lines (e.g., Lagg et al., 2017; Leenaarts et al., 2012, and references cited therein). Therefore, the spectroscopic, imaging, and spectropolarimetric/magnetic observations play a crucial role in understanding various plasma processes (e.g., plasma flows, jet-like ejection, waves, oscillations, etc) coupling the different layers of the solar atmosphere. Such observations are also useful to understand complex structuring of the magnetic fields, such as flux-emerging region, network/inter-network regions, active region/sunspot region, etc. The plasma dynamics from such magnetized regions are substantially studied by imaging, spectroscopic, and spectr-opolarimetric observations. In the Section 2.2, we discuss briefly some space-borne observations and their instruments whose data are utilized in the present thesis.

2.2 Space-based Observatories

In some works outlined in the present thesis, the spectral and imaging data are taken from the space-borne observatories namely Interface Region Imaging Spectrograph (IRIS), and Solar Dynamics Observatory (SDO). We briefly describe their onboard instruments, and observational capabilities in the following subsections:

2.2.1 Interface Region Imaging Spectrograph (IRIS)

Interface Region Imaging Spectrograph (IRIS) [1] is a small NASA explorer space-borne instrument (De Pontieu et al., 2014b) (cf., Fig. 2.1). It was built in the United States by Lockheed Martin Solar and Astrophysics Laboratory (LMSAL) and launched on June 27, 2013. It is a Sun-synchronous observatory. The main objective of IRIS is to better explore the physical processes that take place in the dynamic solar chromosphere and the transition region (TR). This is a magnetically structured and complex layer, which serves as the

[1] http://iris.lmsal.com/data.html

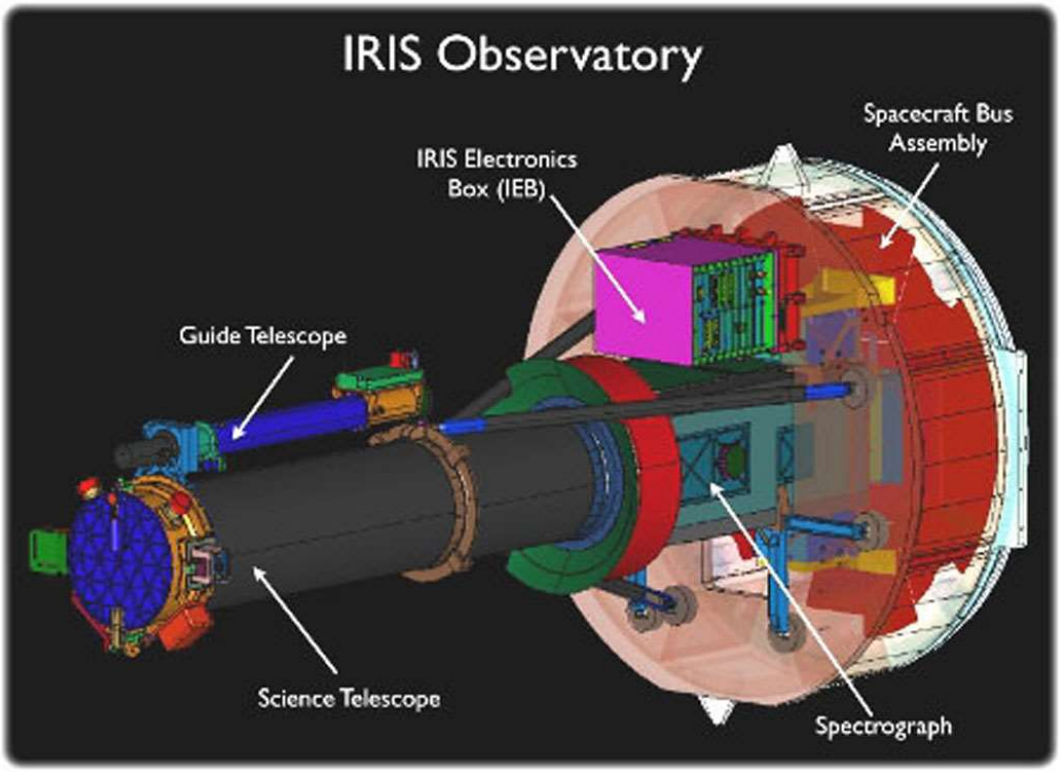

Figure 2.1: Interface Region Imaging Spectrograph (IRIS) with two instruments namely slit-jaw imager, and spectrograph (Credit: LMSAL, NASA/IRIS)

.

interface between the cool solar photosphere and million-degree hot corona (De Pontieu et al., 2014b). IRIS includes a dual-bandpass slit-based image spectrograph, and a 19-cm ultra-violet telescope, which provide the imaging and spectral data. It operates by allowing light coming from the Sun to enter the telescope and fall on a prism with a reflection coating and a long slit of $0.3'' \times 175''$. The light is subsequently directed to the slit-jaw imager by the reflective coating. The light passing through the slit disperses and sends the light to the collimator mirror. The dispersed light is divided into it's two constituents (i) far ultraviolet (FUV) (i.e., wavelength ranges between 1332-1407 Å), (ii) and near ultraviolet (NUV) (i.e, wavelength ranges between 2783-2835 Å). These FUV and NUV spectrograph beams are then routed via various gratings and mapped onto different CCDs. In accordance

with this mechanism, the secondary mirror's direction is modified to scan the surface of the Sun, and obtaining observations by IRIS raster scan. In the present thesis, we used the IRIS slit-jaw-imager (SJI) and spectraographic observational data to study the network jet as reported in Chapter 5.

The IRIS slit-jaw imager (SJI) records temporal image data in four different UV bandpass of the field-of-view (FOV) of 175″×175″ (De Pontieu et al., 2014b). Each wavelength is sensitive to different temperatures of the plasma. The four wavebands and corresponding ions are respectively 2830 Å (Mg II wing), 2796 Å (Mg II k), 1330 Å (C II), 1400 Å (Si IV) at the formation temperature of these lines as 6,000 K, 15,000 K, 30,000 K and 80,000 K. These spectral lines are formed at different heights covering from solar photosphere to the transition region (cf., Table 2.1). The FUV lines, i.e., C II, and Si IV are formed in the upper chromosphere and solar transition region respectively. Their corresponding formation temperatures lie between log T = 3.7 - 5.2. While, NUV lines i.e., Mg II k and Mg II h are formed in the upper photosphere and upper chromosphere respectively. Their corresponding formation temperature lie between log T = 3.7 - 4.2. (cf., Table 2.1).

The main objective of the IRIS is to understand about kinetic energy produced in the interface zone that drives solar activity and turning into radiation and heat. The coronal heating and supersonic solar wind cause a tiny amount of energy to escape from the interface region where the plasma beta (β) (i.e., the ratio of gas pressure to the magnetic pressure) change from very low to high. Therefore, IRIS makes it possible to connect with previous solar missions and including additional information that were focused on spectral lines formed in the mega-Kelvin hot solar corona. In addition to other broad scientific goals, we gain improved understanding of non-thermal energy fueling into the solar atmosphere and solar wind by utilising the spectral data from the dynamic chromosphere and transition region taken by IRIS observations. However, It also performs the studies on spectroscopic

diagnostics of the solar plasma that provide the data about velocity, turbulence, non-thermal energy, and density. In conclusion, IRIS is a cutting-edge space-borne observatory for high spatio-temporal resolution observations, which further supported by stringent including MHD simulation codes, and massively parallel supercomputers (De Pontieu et al., 2014b). This contributes to the growing understanding of the plasma and energy transfer from the transition region and chromosphere which we called interface region particularly.

Table 2.1: IRIS observations in different passband with corresponding ions and temperature (Credit: LMSAL, NASA/IRIS).

Pass band	Wavelengths (Å)	Ions	FOV ($''\times''$)	log T
NUV	2820	Mg II wing	175 × 175	3.7-3.9
FUV 1	1355.6	O I	175 × 175	3.8
NUV	2803.5/ 2796.4	Mg II h/ Mg II k	175× 175	4.0
FUV 1	1334.5/ 1335.7	C II/ C II	175× 175	4.3
FUV 2	1402.8/ 1393.8	Si IV/ Si IV	175× 175	4.8
FUV 2	1399.8/ 1401.2	O IV/ O IV	175× 175	5.2
FUV 1	1349.4	Fe XII	175× 175	6.2
FUV 1	1354.1	Fe XXI	175× 175	7.0

2.2.2 Solar Dynamics Observatory (SDO)

Solar Dynamics Observatory (SDO) (Pesnell et al., 2012) is a NASA space mission that is a part of the Living With Stars (LWS) program. It was sent-off in space in circular geosynchronous orbit at 35,789 km at 102^o west longitude incline at 285^o on February 11, 2010 from the Kennedy Space Center in Florida, USA. It weighed 3000 kg at the time of the launch. It had dimensions of 4.7 m, and contained 6.6 m^2 solar arrays capable of producing 1500 W of power. It started providing the observational data on May 1, 2010. SDO's main scientific objectives are to deeply understand the solar variations and Sun-Earth connection. It also aims to study the magnetic field of the Sun's surface and it's physical mechanisms for releasing magnetic energy into the heliosphere. It consists of (i) the Atmospheric Imaging Assembly (AIA), (ii) the Helioseismic and Magnetic Imager (HMI), as well as

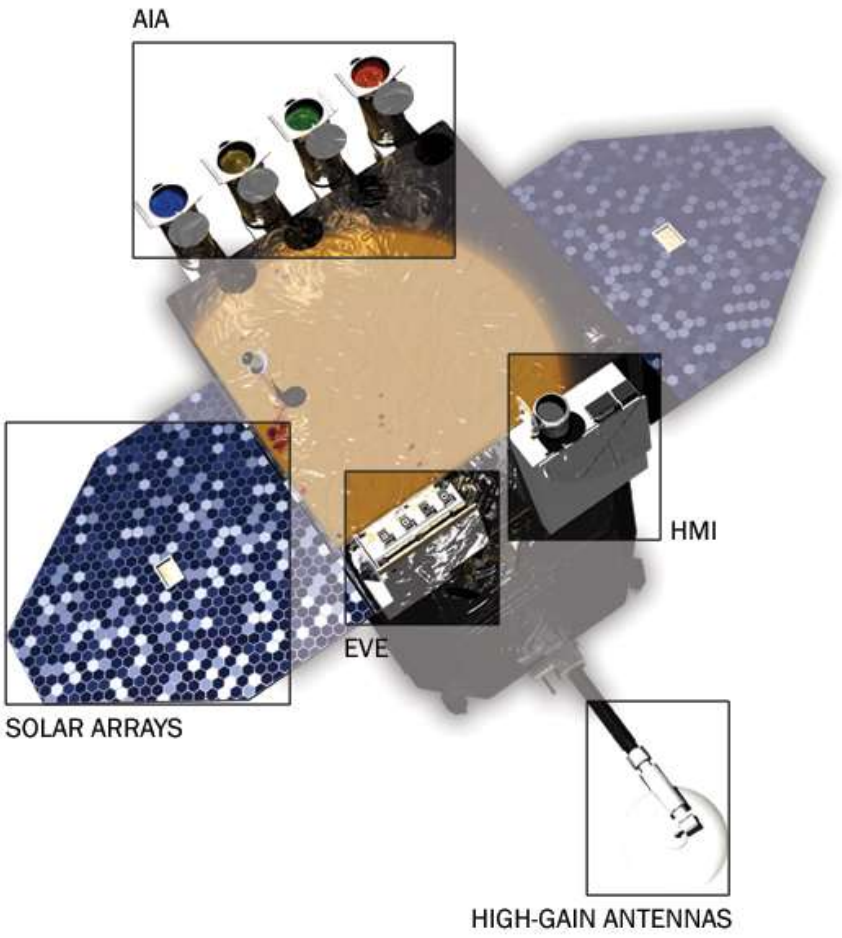

Figure 2.2: Solar Dynamics Observatory (SDO) spacecraft with it's three instruments i.e., AIA, EVE, and HMI (Credit: NASA/SDO).

(iii) the Extreme ultraviolet Variability Explorer (EVE) each of which is dedicated to a specific scientific investigation. AIA and EVE are specified for the investigation of the energy radiated in the UV and EUV wavelength range, while HMI is used to study the variations in the magnetic field of the Sun. HMI also provides the measurement of the internal motions which is accountable for the generation of the magnetic field. It is capable of measuring the helioseismic and line-of-sight (LOS) magnetic fields. SDO provides the

high-resolution data, with a primary focus on understanding various transients event such as solar jets, flares, CMEs, prominence eruption, etc. The solar images are captured on a CCD with 4096 x 4096 pixels. Figure 2.1 displays a view of SDO spacecraft and its onboard instruments AIA, EVE and HMI. The Full resolution data from AIA and HMI instruments are freely available on the Joint-SOC (JSOC) Stanford website [2]. In the next subsection, we describe the AIA instrument of SDO whose data is used in this thesis to understand the onset and properties of the K-H instability (see Chapter 7).

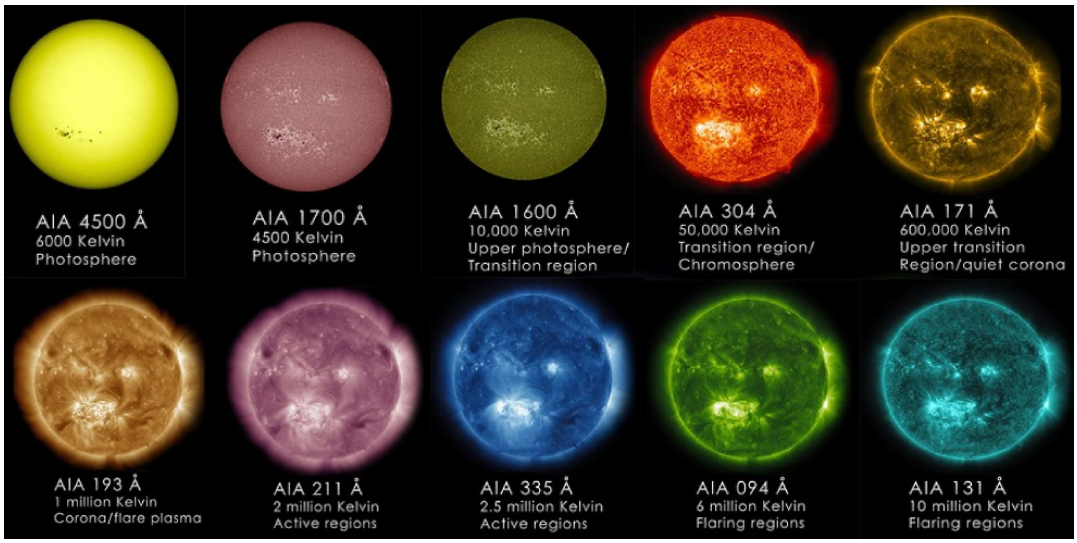

Figure 2.3: SDO/AIA observation of the Sun's atmosphere in EUV/UV and visible wavebands. (Credit: NASA/SDO).

Atmospheric Imaging Assembly (AIA)

AIA provides the multiwavelength, full disk temporal images data of the Sun (Pesnell et al., 2012). It is made up of an array of 4 telescope of 20 cm primary mirror with 1.2″ pixel-resolution and a secondary mirror for each telescope. The field of view (FOV) of each 20 cm telescope is 41′ circular diameter which provides the full-disk images on 4k × 4k CCD. It's temporal resolution (i.e., cadence) is 12 second. It provides the images of the solar atmosphere for ten wavelength bands in Visible/UV/EUV. These wavelength bands

[2] http://jsoc.stanford.edu

Table 2.2: The details of Visible, UV and EUV channels of SDO/AIA instrument with the primary emitting ions and their formation temperature in the solar atmosphere (Credit: NASA/SDO)

.

Primary ion(s)	log T	Channel	Region of Sun's atmosphere
continuum	3.7	4500 Å	photosphere
continuum	3.7	1700 Å	temperature minimum, photosphere
continuum, C IV	5.0	1600 Å	upper photosphere, transition region
He II	4.7	304Å	chromosphere, transition region
Fe IX	5.8	171 Å	quiet corona, upper transition region
Fe VIII, XXI	5.6, 7.0	131 Å	transition region, flaring corona
Fe XII, XXIV	6.3, 7.3	193 Å	corona and hot flare plasma
Fe XIV	6.3	211 Å	active-region corona
Fe XVI	6.4	335 Å	active-region corona
Fe XVIII	6.8	94 Å	flaring corona

depict different regions/temperature as well as a verity of plasma dynamics and processes occurring in the solar atmosphere (cf., Fig 2.3, Table 2.2). The EUV/UV emission captured by various filters of AIA are specified for specific spectral lines. The hot coronal plasma is studied by using these lines, e.g., Fe XVIII (94 Å), Fe VIII, XXI (131 Å), Fe IX (171 Å), Fe XII, XXIV (193 Å), Fe XVI (335 Å), Fe XIV (211 Å). The transition region plasma is characterized by He II (304 Å). In particular, AIA 304 Å describes supergranules in the quiet-Sun region and corresponds to the upper chromospheric as well as TR emission. The C IV (near 1600 Å) and the nearby continuum (1700 Å), and continuum (4500 Å) provide the information about cool, dark photospheric features associated with sunspots and the bright emission associated with the plage regions. In conclusion, SDO/AIA records the full disk imaging data covering different dynamical motions, eruptive/transients processes, waves/oscillations coupling the solar photosphere to the outer corona. The dimensions of particular data set of AIA image are 480×360 pixels, or $288'' \times 216''$.

The data taken from AIA/SDO is utilized to understand the detailed dynamics of different plasma/magnetic structuring occurring in the Sun's atmosphere. The magnetized plasma serves as a source of energy dissipation for various activities in the solar atmosphere.

The large eruptions, confined plasma flows, solar jets, waves, and oscillations are all caused by the ongoing magnetic field re-organization or associated plasma motions. Therefore, the multiwavelength, high-resolution observations from AIA, provide deep understanding of the evolution, and triggering mechanism of various transients/eruptive processes. In the present thesis, we studied the of Kelvin-Helmholtz (K-H) instability in the cool counterpart of the coronal jet using multiwavelength observations taken by AIA (see Chapter 7). The imaging data taken in different EUV wavebands are analysed and interpreted using imaging, distance-time, DEM analysis of the region-of-interest (i.e., K-H unstable jet in the fan-spine topology) in Chapter 7 of the thesis.

2.3 Data Analysis Techniques

The present thesis focuses on the study of cool jets and associated plasma processes such as waves, shocks, transverse oscillations, flows, and the evolution of K-H instability. Therefore, we utilize various data reduction techniques to collect the physical information present in the observational data employed in some particular chapters of this thesis (Chapter 5 & 7). In this section, we briefly discuss the data analysis techniques, which help us to calibrate the data, and extract out various parameters and characteristics of the localized solar atmosphere, and dynamical plasma processes there.

2.3.1 Image calibration and data processing

The initial calibration of the imaging data taken from SDO/AIA and IRIS/SJI instruments are done as follows:

- The raw elementary data are flat-fielded, rebinned, and processed to eliminate spikes and bad pixels.

- After eliminating the defective pixels and flat field adjustments from the elementary data, we obtain level 1.0 and level 1.5 data (in form of significant observations) in FITS file format.

- The physical characteristics (e.g., pixel size, direction, center coordinates) saved in the keyword form. The Solar soft packages possess image calibration routines (such as aia_prep) that are used to normalise the data, updating the header, and perform basic calibration such as rotation, translation, and scaling.

- It updates all stored keywords of images in accordance with the reference image, using which all the images are aligned. Additionally, it aids in the alignment of the images taken with various instruments of varying spatial resolution.

- These updated images are also enhanced by applying different operations on them. For easier comprehension of the data, it may be altered, scaled to our preferences, and coloured differently.

- To get scientific conclusions, these updated images and calibrated data are then analysed with different procedures discussed later in this chapter.

We utilize Si IV 1330 Å IRIS SJI image data to obtain the signature of spicule-like cool jets in the lower solar atmosphere. Their details are discussed in Chapter 5. We use multi-wavelength SDO/AIA temporal image data in obtaining scientific results related to the K-H instability as outlined in Chapter 7.

2.3.2 Spectral analysis

The IRIS spectral data is used in Chapter 5 to estimate the velocity enhancements as evident from Si IV 1393.755 Å line profiles. In general, IRIS spectral data contains three types of emission lines namely (i) absorption line, (ii) optically thick emission line, and

(iii) optically thin emission lines. We utilize only an optically thin line, i.e., Si IV emission line in Chapter 5. In our study we understand the dynamics of the spicule-like jets visible in the transition region emissions. This line is distinguished mostly by a single peak profile. However, in our case the double peaked Si IV line profile is obtained to further analyse and measure the velocity enhancements. We removed the orbital variation effects on this line before fitting it using the iris SSW routines [3]. We employ Gaussian fitting to line of Si IV to obtain the fundamental parameters of the line profiles. The details of the spectral analysis of Si IV 1393.755 Å line profiles are outlined in Chapter 5.

2.3.3 Differential emission measure (DEM) analysis

A wide range of the plasma temperature is covered by a variety of emissions from the solar atmosphere. In this order, a board range of UV/EUV emissions from the solar atmosphere are in thermal equilibrium and essentially optically thin. A method called DEM can be utilized to determine the density and temperature structure of the multi-thermal plasma in the atmosphere of the Sun. The DEM is expressed as (Cheung et al., 2015),

$$DEM(T) = \int n_e^2(h(t))\frac{dh}{dT} \tag{2.1}$$

where $DEM(T)$ represents the DEM at a plasma temperature $'T'$ and at a depth of $'h'$ along the line-of-sight, $n(h(T))$ depicts the density of electron at temperature T at a depth of h. In general, DEM can be performed by utilizing various techniques/methods (e.g., Sparse Inversion Method, Regularized Inversion Method, etc) to estimate the thermal and density structures of various transients and eruptive events as well as their associated plasma dynamics in the inner solar corona. In the present thesis, we used the Sparse Inversion Method to estimate the thermal and density structures of the localized corona

[3] iris_orbitvarr_corr_12.pro

where the jet-like plasma flows occur above a fan spine topology in the jet-like plasma ejection (cf., Chapter 7).

Sparse Inversion Method

The sparse inversion algorithm, developed in IDL and accessible in Solar soft, is an inversion method to obtain the DEM (Cheung et al., 2015). This approach utilizes a simple function to obtain the solutions from the optically thin emissions captured by SDO/AIA multifilter image data by minimising the total emission measure (EM). This scheme, which uses Chi-square (χ^2) reduction, is perfect for an over-determined systems. However, the over-fitting and under-determined system with χ^2 minimum arises. The sparse inversion method only offers the positive response between maximum (0,I-tol) and minimum (0,I+tol), where I represents the reconstructed intensity, and tol depicts the reconstructed intensity tolerance (Cheung et al., 2015). The sparse inversion method sustains for the temperature range between 5.5≤log T≤7.7 with an interval of Δlog T=0.1 (Cheung et al., 2015). Using this method, we perform the DEM with six AIA EUV filters, i.e., 94 Å, 131 Å, 171 Å, 193 Å, 211 Å, and 335 Å which are optically thin as outlined in Chapter 7. The estimation of mean temperature from the DEM was made by the following expression (Cheung et al., 2015):

$$T_{mean} = \frac{\int_{T_{min}}^{T_{max}} DEM(T) T dT}{\int_{T_{min}}^{T_{max}} DEM(T) dT} \tag{2.2}$$

The number density (n) from the emission measure is calculated by (Cheung et al., 2015),

$$n = \sqrt{\frac{EM}{h}}, \tag{2.3}$$

where "h" represents the depth of the area from where the emissions came from. It is assumed that the depth and width of the area along the LOS are equal.

In conclusion, these different methodologies/techniques are used to find out physical characteristics of the emitting plasma from the imaging and spectral observational data recorded by different space-borne instruments (Chapter 5 & 7). The dynamics of the complicated interactions between magnetic fields and plasma are investigated using scientific interpretation of the data obtained form these instruments. In the next sub-section, we briefly describe the numerical simulation method (i.e., PLUTO code), which is used to model the cool jets. We only discuss those features of PLUTO that we utilize in our models presented in the thesis, and the full details of the PLUTO code can be found in Mignone et al. (2007a)

2.4 Numerical Methods

2.4.1 Magentohydrodynamic (MHD) system

We take basic MHD equations in their conservative form to numerically model the evolution and generation of cool jet like plasma ejections in the magnetized, gravitationally stratified, and longitudinally structured solar atmosphere. These equations are outlined as follows (e.g., González-Avilés et al., 2021; Mignone et al., 2007b; Singh et al., 2019; Srivastava et al., 2020):

$$\frac{\partial \rho}{\partial t} + \nabla \cdot (\rho \mathbf{v}) = 0, \tag{2.4}$$

$$\frac{\partial (\rho \mathbf{v})}{\partial t} + \nabla \cdot (\rho \mathbf{v}\mathbf{v} - \mathbf{B}\mathbf{B} + p_T \mathbf{I}) = \rho \mathbf{g}, \tag{2.5}$$

$$\frac{\partial \mathbf{B}}{\partial t} + \nabla \cdot (\mathbf{v}\mathbf{B} - \mathbf{B}\mathbf{v}) = 0, \tag{2.6}$$

$$\nabla \cdot \mathbf{B} = 0, \tag{2.7}$$

$$\frac{\partial E}{\partial t} + \nabla \cdot ((E + p_T)\mathbf{v} - \mathbf{B}(\mathbf{v} \cdot \mathbf{B})) = \rho \mathbf{v} \cdot \mathbf{g} + Q_{rad} + \nabla \cdot q, \tag{2.8}$$

and

$$p = \frac{k_{\rm B}}{m}\rho T \tag{2.9}$$

where ρ represents the mass density of the plasma fluid, **v** the plasma velocity. The symbol **B** is depicting the magnetic field, which satisfy the divergence-free condition. The symbol p is considered as the thermal pressure of the plasma, at a given temperature T. The $k_{\rm B}$ is the well known Boltzmann constant, and m describes the mean mass of the plasma particles in the fully ionized configuration. In our simulations (Chapters 3-6), we adopt a value of $m = 1.24$ for the given model solar atmosphere. We neglect other non-ideal physical effects e.g., The magnetic diffusivity, dissipative effects, viscosity and resistivity, and heating of the plasma in the models outlined in Chapter 3, 4, and 6, while we consider the radiative and thermal conduction losses in the model described in Chapter 5. We do not take into account background velocity of the plasma flows at equilibrium. The PLUTO code, which is used to solve magnetohydrodynamic equations in their conservative form also obeys the ideal gas law (Mignone et al., 2007a). The symbol $p_T = p + B^2/2\mu$ is the total pressure which is the sum of gas and magnetic pressure due to the embedded magnetic field. $\hat{\mathbf{I}}$ is a 3×3 unit matrix in the Euclidean space. In addition, the expressions like **vB** demonstrates 3×3 dyadic tensor. The symbol E infers the total energy density (e.g., Mignone et al., 2007a; Singh et al., 2019; Wołoszkiewicz et al., 2014):

$$E = \frac{p}{\gamma-1} + \frac{\rho v^2}{2} + \frac{B^2}{2\mu}. \tag{2.10}$$

The symbol μ denotes the magnetic permeability. The specific heat ratio γ is given as $5/3$. The gravitational term in Eqs. (2.5) & (2.8) is constructed as **g** = [0, -g, 0] with its value 274 m s^{-2} at the solar surface.

We consider the following term for the non-adiabatic atmosphere:

$$Q_{rad} = -n_H^2 \Lambda(T), \tag{2.11}$$

which is an optically thin radiative loss estimated using the CHIANTI code (Landi et al., 2012). It considers the number density of hydrogen of the order of 10^9 cm^{-3}, and ionization equilibrium is implemented as mentioned in Dere et al. (2009). The radiative energy losses are consistent physically to an optically thin plasma such as upper chromosphere/Transition region, and the inner solar corona where the jets are formed and propagate. We exclude the photospheric and low chromospheric cooling by setting $\Lambda(T)$=0 for T<1×10^4 K. In addition, we consider the thermal conduction in the model as described in Chapter 5, in form of the heat flux vector that permits the propagation of heat along the magnetic field lines, and it is mentioned in González-Avilés et al. (2021):

$$\mathrm{q} = \kappa_{\parallel} \hat{\mathrm{b}} (\hat{\mathrm{b}} \cdot \nabla T). \tag{2.12}$$

Here, $\kappa_{\parallel}$ is the coefficient of the thermal conduction parallel to the magnetic field lines. The $\hat{\mathrm{b}}$=B/|B| is the unit vector directed along the magnetic field lines. We take into account the thermal conduction coefficient as reported for the fully ionized plasma by Spitzer (1962), which is given as follows:

$$\kappa_{\parallel} = \kappa_o T^{5/2}. \tag{2.13}$$

We consider the value of κ_o as 1×10^{-6} ergs cm^{-1} s^{-1} K$^{-7/2}$ (Spitzer, 1962).

We adopt the set of ideal MHD equations from Eqs. 2.4-2.9 without adding cooling effects of radiation (Eq. 2.11) and thermal conduction term ($\nabla \cdot q$) in Eq. 2.8. The resulting set of MHD equations represent the ideal (adiabatic) atmosphere at MHD scales used in Chapters 3, 4, & 6. The present thesis aims to model the cool jet-like plasma processes in ideal MHD regime (Chapters 3,4 & 6) and non-ideal regime (Chapter 5). Furthermore, the

set of MHD equations that in form of the partial differential equations (Eqs. 2.4-2.9) are solved by implementing several numerical methods as embedded in the PLUTO code (e.g., Mignone et al., 2007a). Some details, which are used in our simulations, are described in various forthcoming subsections.

2.4.2 Structure of PLUTO code

The PLUTO [4] is a (finite-difference/finite volume) Godunov type code. This code is used to simulate the MHD, equations (Mignone et al., 2007a). It is based on the conservation of laws and can represent high resolution multi-physics, multi-solver, and multi-algorithm numerical simulations. It is appropriate for the time-dependent, and explicit calculations of supersonic fluid flows with significant discontinuities. In the present thesis, it is used in understanding the dynamics and flows of magnetised solar plasma (Mignone et al., 2007a). PLUTO is fully developed in the language of C programming. It may work on either at a single processor or over the parallel computers. The later process can be employed using the Message Passing Interface (MPI) libraries (e.g., Mignone et al., 2007a). The PLUTO code includes several routines, e.g., mapper routines for converting primitive to conservative variables and vice-versa, a flux routine, a source term function, and a routine that computes the characteristic speeds of the Jacobian matrix in the given domain at their maximum and minimum values. (Mignone et al., 2007a). Furthermore, by utilising the independent modularity, required functionality may be readily implemented. In addition, the specific configuration is defined in an extra Python language based on the needs of the user. Different problem-based features and techniques, such as physics module, number of dimensions, domain, geometry, various reconstruction methods, time stepping integration, and so on, are specified in this script (Mignone et al., 2007a). PLUTO has solved the set of MHD equations (Eqs. 2.4-2.9) by integrating a system of conservation laws (in our case

[4] http://plutocode.ph.unito.it/download.html

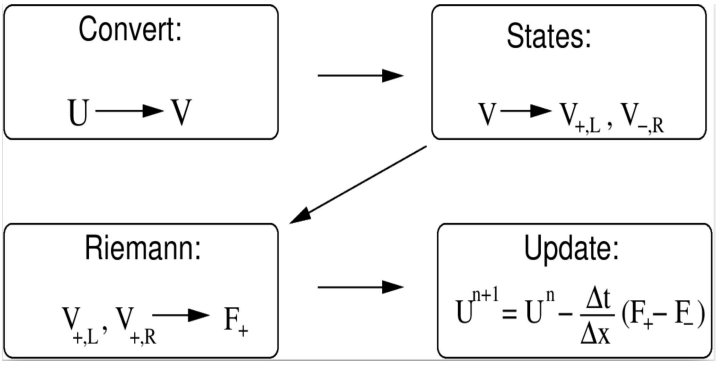

Figure 2.4: The reconstruct-solve-average (RSA) approach is depicted in a flow chart as originally given in Mignone et al. (2007a). Top-left: Volume averages (**U**) is easily converted into primitive variables (**V**). Top-right: The left and right states are respectively represented by ($\mathbf{V}_{+,L}$) and ($\mathbf{V}_{-,R}$) using either extrapolation or interpolation of appropriate variables. The solution is therefore advanced and updated in time by solving a Riemann problem between states ($V_{+,L}$) and ($V_{-,R}$). It further computes the numerical flux function (F_+) at various interfaces of the given cell (Mignone et al., 2007a). This scheme is adopted from the master paper of PLUTO by Mignone et al. (2007a).

MHD equations), which can be represented in a general form as follows (Mignone et al., 2007a):

$$\frac{\partial \mathbf{U}}{\partial t} = -\nabla \cdot \mathbf{T}(\mathbf{U}) + \mathbf{S}(\mathbf{U}), \tag{2.14}$$

Here **U** shows the state of conserved variables, **T**(**U**) represents the rank-2 tensor of flux variables of each component, and **S**(**U**) represents the source terms.

The explicit form of **U**, **V**, **T**(**U**) and **S**(**U**) is based on the choice of specific physical module. In our MHD simulation, therefore, a physics-based module along with governing set of MHD equations (Eqs. 2.4-2.9) and the set of the algorithms required to compute the terms involved in the discretization of the right hand side of most general form those equations (cf., Eqs 2.14) of Eq. (2.14) are utilized (Mignone et al., 2007a). The set of ideal MHD equations (Eqs. 2.4-2.9) are incorporated in the PLUTO code as (Mignone et al.,

2007a):

$$\mathbf{U} = \begin{pmatrix} \rho \\ \mathbf{m} \\ \mathbf{B} \\ E \end{pmatrix} \quad T(\mathbf{U}) = \begin{pmatrix} \rho\mathbf{v} \\ \mathbf{mv} - \mathbf{BB} + p_{\mathrm{t}} I \\ \mathbf{vB} - \mathbf{Bv} \\ (E + p_{\mathrm{t}})\mathbf{v} - (\mathbf{v}\cdot\mathbf{B})\mathbf{B} \end{pmatrix}^{\mathrm{T}}, \tag{2.15}$$

Here, 'ρ' depicts the mass density. The $\mathbf{m} = \rho\mathbf{v}$ and $p_{\mathrm{t}} = p + |\mathbf{B}|^2/2$ depict respectively mass flux and the total pressure. The symbol "E" represents the total energy which is defined as:

$$E = \frac{p}{\Gamma - 1} + \frac{1}{2}\left(\frac{|\mathbf{m}|^2}{\rho} + |\mathbf{B}|^2\right). \tag{2.16}$$

Here, vector fields such as $\mathbf{B} \equiv (B_1, B_2, B_3)^{\mathrm{T}}$, $\mathbf{m} \equiv (m_1, m_2, m_3)^{\mathrm{T}}$, and $\mathbf{v} \equiv (v_1, v_2, v_3)^{\mathrm{T}}$, depict the magnetic field, momentum density, and velocity. The symbol Γ describes the ratio of specific heats for the ideal gas.

2.4.3 Solenoidal constraint

In order to solve the MHD equations, the condition for the solenoidal constraint ($\nabla \cdot \mathbf{B} = 0$) should satisfy for the complete run time of the simulation. In general, unless specific discretization techniques are utilized, numerical schemes are unable to naturally preserve this criterion. In the PLUTO code, there are different schemes for the magnetic mono-pole control such as: (i) the eight wave formulation (Mignone et al., 2007a), (ii) the constrained transport (CT) (Mignone et al., 2007a).

In the eight wave formulation, the magnetic field is taken on the cell centre and the MHD equation include an extra source term. This characteristic, which can be differ depending on the Riemann solver, considerably enhances the robustness of the code. In the CT scheme, the magnetic induction equation of MHD is being directly integrated by

Table 2.3: Coordinate systems implemented in the PLUTO code regarding the position coordinates, volumes and areas and their meanings in the Cartesian coordinate system (Credit: Mignone et al. (2007a))

PLUTO	$x1$	$x2$	$x3$	Δ^1	Δ^2	Δ^3	A^1	A^2	A^3
Cartesian	x	y	z	Δx	Δy	Δz	1	1	1

implementing Stokes's theorem, and the magnetic field follows a staggered collocation. The details can be found in various literatures (e.g., Mignone et al., 2007a))

2.4.4 Notations and grids

In our simulation, we use the Cartesian coordinate system which is adopted in the PLUTO code using different symbols. The meaning of the coordinate in PLUTO and Cartesian coordinate is represented by Table 2.3.

Here, $x1$, $x2$, $x3$ represent the position coordinates, Δ^1, Δ^2, Δ^3 the volume coordinates, and A^1, A^2, A^3 the interface area that is equal to unity. PLUTO adopt generic orthogonal curvilinear coordinates and logically rectangular grids. We assume that N_1, N_2 and N_3 are being the number of points in x, y & z direction. The upper and lower coordinate bounds of the zone $(i,\ j,\ k)$ are respectively $(\mathrm{x1}_{i+},\ \mathrm{x2}_{j+},\ \mathrm{x3}_{k+})$ and $\mathrm{x1}_{i-},\ \mathrm{x2}_{j-},\ \mathrm{x3}_{k-})$. The number of points i.e., N_1, N_2 and N_3 are defined as $1 \le i \le N_1$, $1 \le j \le N_2$, $1 \le k \le N_3$. The width of each zone is expressed as $\Delta x1_i = x1_{i+} - x1_{i-}$, $\Delta x2_j = x2_{j+} - x2_{j-}$, $\Delta x3_k = x3_{k+} - x3_{k-}$. The spacing between two nearest zones can be either uniform or stretched. The stretched one can be either geometrical or logarithmic. Therefore, the division of cells (i.e., grids) in the PLUTO code, is estimated by these upper and lower coordinates of the bound zone, i.e., $(i,\ j,\ k)$. In case the of three-dimensional physical quantities, the PLUTO code adopted the specific notation. In such a case, we assume that $\mathbf{V}_{i,j,k}$ becomes simply $\mathbf{V}$. Therefore, the two-point difference of the operator in the one-dimension is expressed by Mignone

et al. (2007a) as follows:

$$\mathcal{L}^d(\mathbf{V}) = -\frac{1}{\Delta^d}\left(A^d_+\mathbf{F}^d_+ - A^d_-\mathbf{F}^d\right) + \mathbf{S}^d \tag{2.17}$$

Here, $d = 1,2,3$ represent the direction respectively in x, y, z. The Δ^d and $A^d_\pm$ represent the cell volume and interface area of cell's right (+) and left (-) respectively (cf., Table 2.3). Here, $\pm \equiv (i\pm, j, k)$, $(i, j\pm, k)$, $(i, j, k\pm)$ when $d = 1,2,3$ i.e., (x, y, z) respectively. In case of algorithm of 1-D quantities, we will also remove the superscript 'd' because it is not required. The numerical flux functions $\mathbf{F}_\pm$ in Eq. (2.17) expressed as (Mignone et al., 2007a):

$$\mathbf{F}_+ = \mathcal{R}(\mathbf{V}_{+,\mathrm{L}}, \mathbf{V}_{+,\mathrm{R}}) \tag{2.18}$$

Here, $\mathbf{V}_{+,L}$ and $\mathbf{V}_{+,R}$ represent the left as well as right states at the edges of the zone normal to the x-direction. Symbol $\mathcal{R}$ represents the Riemann solver by which PLUTO solves Eq. (2.17). We briefly describe Riemann problem in subsection 2.4.6.

2.4.5 Reconstruction

To avoid spurious oscillations at discontinuities and steep slopes, reconstruction procedure must be used with monotonicity criterion in order to solve the MHD equations. PLUTO code reconstruct the piece-wise polynomial approximations using the interpolation method. The interpolation routines are available in the PLUTO code. Taking into account the approximation of the piece-wise $\mathcal{P}(\mathbf{x})$ polynomial to $\mathbf{V}$ within each grid (or cell), beginning with its grid averages (Mignone et al., 2007a), we can write:

$$\mathbf{V}_{\pm,\mathrm{S}} = \mathcal{I}\left(\vec{\mathcal{P}}, \mathbf{V}\right), \tag{2.19}$$

Here, L=S, (or R=S) at $\mathbf{x}$=$\mathbf{x}_+$ (or $\mathbf{x}$=$\mathbf{x}_-$). The symbol "$\mathcal{I}$" represents an interpolation algorithm that provides right and left edge interpolated values within each grid or cell, i.e., $\mathbf{V}_{-,R} = \lim_{\mathbf{x}\to\mathbf{x}_-} \mathcal{P}(\mathbf{x})$ and $\mathbf{V}_{+,L} = \lim_{\mathbf{x}\to\mathbf{x}_+} \mathcal{P}(\mathbf{x})$. Symbol "R" and "L" subscripts depict the right and left sides of the grid interface.

For the second-order linear interpolation, the reconstructions of polynomial is expressed by Mignone et al. (2007a) as follows:

$$\mathbf{V}_{\pm,S} = \mathbf{V} \pm \frac{\Delta\tilde{\mathbf{V}}}{2}, \tag{2.20}$$

Here, $\Delta\tilde{\mathbf{V}}$ represents a slope generated in the PLUTO code using a limiting process applied to the primitive variables of the MHD Eqs.

$$\Delta\tilde{\mathbf{V}} = \sum_k \Delta\tilde{w}_k \mathbf{r}_k\,, \quad \Delta\tilde{w}_k = \lim\left(\Delta w_{k,+}, \Delta w_{k,-}\right), \tag{2.21}$$

Here, $\Delta w_{k,\pm} = \pm\mathbf{l}_k \cdot (\mathbf{V}_{i\pm1} - \mathbf{V}_i)$ were forward (+) as well as backward (−) derivatives, where k defines the k-th characteristic field. The symbols $\mathbf{l}_k$ and $\mathbf{r}_k$ respectively represent the left and right eigenvectors of the primitive variables of the set of MHD equations in PLUTO code (Mignone et al., 2007a).

PLUTO permits to select either 1^{st} order in space (i.e., flat), or 2^{nd} order (i.e., linear), or 3^{rd} order convex ENO (i.e., parabolic reconstructions) for the MHD equations (Del Zanna and Bucciantini, 2002; Mignone, 2005; Mignone et al., 2007a).

2.4.6 Riemann solver

In PLUTO, the set of MHD equations can be solved using Riemann solvers, which is of different type, e.g., HLLD (Miyoshi and Kusano, 2005), HLLC (Li, 2005), HLL (Janhunen, 2000), the Roe solver (Cargo and Gallice, 1997), and the Lax-Friedrichs solvers. The numerical flux function $\mathbf{F}_+$ at the edge of the zone (x_+) required to solve the initial value

problem **U**(x,t), for $t > t_0$ (Mignone et al., 2007a)

$$\mathbf{U}(x,t_0) = \begin{cases} \mathbf{U}_{+,L} & if \quad x < x_+ , \\ \\ \mathbf{U}_{+,R} & if \quad x > x_+ , \end{cases} \tag{2.22}$$

It can be difficult to accomplish the exact solution to the designated Riemann problem (2.22), which requires the decay of a number of the non-linear waves. Existing Riemann solvers frequently use the upwind methods, which are based on various levels of approximation, with the exceptions of a few basic circumstances.

In the order to solve the Riemann problem, there are several methods (e.g., Lax-Friedrichs Rusanov method, HLL family method, Linearized Riemann method, Advection Upstream Splitting Method, Roe solver, etc) that can be adopted to solve the flux function 2.22 (e.g., Cargo and Gallice, 1997; Janhunen, 2000; Li, 2005; Mignone et al., 2007a; Miyoshi and Kusano, 2005, and references citet theirin). These methods are accessible for all physics modules (e.g., HD, MHD, RMHD, etc) in the PLUTO (Mignone et al., 2007a). In our simulation, we utilize the Roe solver (Mignone et al., 2007a) to compute the flux function of the Riemann problem (Eq. 2.22).

Roe Solver Method

The Roe solver solves the flux function which is expressed as (Cargo and Gallice, 1997; Mignone et al., 2007a):

$$\mathbf{F} = \frac{1}{2}\left[\mathbf{f}_L + \mathbf{f}_R - \sum_k |\lambda_k| \mathbf{L}.(\mathbf{U}_L - \mathbf{U}_R)\mathbf{R}_k\right], \tag{2.23}$$

Here, the rows (columns) of **L** and **R** respectively represent the left and right eigenvectors of the Jacobian $\partial\mathbf{f}(\mathbf{U})/\partial\mathbf{U}$. The symbol $|\lambda_k|$ depicts the velocity of the local signal.

Various physics modules have varying sets of the Riemann solvers, and other techniques of these solutions are easily designed there in the code. In our simulation, we compute more precise Riemann solver such as Roe solver which is linearized and precise method to solve the inadequate numerical dissipation. The detailed of the Riemann solver in case of different physics module is given in Quirk (1994) and Mignone et al. (2007a).

2.4.7 Temporal evolution

PLUTO adopt the temporal evolution which is the discretization of Eq (2.14, left hand side). This method can be used for all the physics module in the PLUTO code. The discretization of the Euler Eq. is described by Mignone et al. (2007a):

$$\frac{\mathbf{U}^{n+1} - \mathbf{U}^{n}}{\Delta t} = \mathcal{L}^{n}, \tag{2.24}$$

Where, for dimensionally split or unsplit schemes, operator $\mathcal{L}^n$ represents the operator at right hand side (2.17) or a sum of them, as appropriate. The Δt represents the time step which is approximated by the Courant-Friedrichs Lewy (CFL) condition describe as (e.g., Courant et al., 1928) :

$$\Delta t = C_a \min_d \left(\frac{\Delta l^d_{\min}}{|\lambda^d_{\max}|} \right), \tag{2.25}$$

Here, $\lambda^d_{\max}$ and $\Delta l^d_{\min}$ describe respectively the largest velocity of the signal and smallest length of the cell in the direction d. The $C_{\rm a}$ represents the Courant number. The courant number depends on the different time marching schemes (e.g., MUSCL-Hancock and Characteristic tracing schemes (MH & ChTr), second and third order Runge-Kutta scheme (RK2 & RK3)). In our simulation, we use the RK3 scheme for the calculation of the temporal evolution. RK3 scheme can be utilized for dimensionally unsplit and also for dimensionally split algorithm. The maximum Courant number (C_a) is defined for the RK3 scheme, which equals to $1/\sqrt{N_d}$ for dimensionally unsplit scheme, where N_d describes

the number of dimensions (i.e., N_d = 1, 2, 3), while C_a is equal to 1 for the split algorithm (Mignone et al., 2007a).

PLUTO offered a variety of time-marching algorithms (e.g., completely discrete zone-edge extrapolated method, semi-discrete method) for the explicit numerical integration related to the various conservation law (Eq. 2.14). In our simulation, we use the RK3 scheme which is expressed under semi-discrete method.

Semi Discrete Methods

In this method, the spatial discretization method is examined independently to the temporal evolution. Therefore, Eq. 2.14 is discretized as a standard ordinary differential equation (ODE). In this frame-work, the 3^{rd} order Total Variation Diminishing (TVD) Runge-Kutta (RK3) scheme is used for the temporal evolution. RK3 method has additional steps as compared to RK2 scheme which is expressed as (Mignone et al., 2007a):

$$\mathbf{U}^{*} = \mathbf{U}^{n} + \Delta t^{n}, \tag{2.26}$$

$$\mathbf{U}^{**} = \frac{1}{4}\left(3\mathbf{U}^{n} + \mathbf{U}^{*} + \Delta t \mathcal{L}^{*}\right), \tag{2.27}$$

$$\mathbf{U}^{n+1} = \frac{1}{3}\left(\mathbf{U}^{n} + 2\mathbf{U}^{**} + 2\Delta t \mathcal{L}^{**}\right). \tag{2.28}$$

In this technique, the result of the interpolation routine provides the Riemann solver's input states. In this order, the boundary condition for the specific problem must be assigned prior to each step. The RK3 scheme requires the solution of three Riemann problems grid (or cell) per direction. Additionally, RK3 integrator, which are totally unsplit, needed for a stronger time step limitation (Mignone et al., 2007a).

2.4.8 Source terms and non-hyperbolicity

PLUTO offers to add the several additional features such as centripetal and coriolis terms, external gravity forces, optically thin radiative losses, and non-ideal terms (e.g., thermal conduction, viscosity, and resistivity) etc. These additional terms are called as local source terms which are added either during the advection stage or by operator splitting method. They are the functions of the variables themselves, however, they are definitely not of their derivatives. In our simulation, we have used non-ideal conditions (in particular, the optically thin radiative losses and thermal conduction in Chapter 5) which is subject to the correction in source terms (Mignone et al., 2007a).

In addition, we point-out here about the isotropic pressure term p which is the component of the flux tensor in the momentum equation and expressed as $\nabla \cdot (I_p) \equiv \nabla p$. Pressure differencing terms are evaluated independently as a gradient components. They are never contribute to the source terms in the energy equation. Therefore, we describe the correction methods in source term of the optically thin radiative loss and thermal conduction.

Radiative Cooling

PLUTO code makes use of a radiation cooling module (Mignone et al., 2007a). The radiative cooling effect occurs primarily when the cooling timescale equals or is shorter compared to the standard timescale for the dynamical evolution of the state. The optically thin radiative loss processes are considered as a local source terms that may be affected by the temperature, density, and an arbitrary number of the ions of distinct element (e.g. H, He, C, N, O, etc). In this order, collisional ionisation, recombination, and charge exchange reactions occur in the ionization fractions as they are advected along with the plasma fluid. To develop the chemical network over time, operator splitting is used. In regions of the fast variation, a 2^{nd} order completely implicit scheme is utilized, but a second order explicit integrator was used alternatively.

PLUTO adopt several module for the optically thin radiative loss such as Power law, TABULATED, H2_COOL etc. In our modelling, we adopt TABULATED module which is internal energy equation for the internal energy with a tabulated cooling function expressed as (Mignone et al., 2007a) :

$$Q_{rad} = -n_H^2 \Lambda(T), \tag{2.29}$$

Here, n_H is the hydrogen number density and T depicts the temperature. In this module, there is no chemical network of the ions and other particle present in the simulation domain. This module may utilize for a fixed temperature range according to the science case. In our simulation, we adopt the optically thin radiative loss estimated using the CHIANTI code (Landi et al., 2011). Some details are also discussed in Chapter 5.

Thermal Conduction

Second-order spatial derivatives are introduced by the parabolic terms (e.g., thermal conduction, resistivity, etc.) and their treatment necessitates the solution of that term e.g., thermal conduction which is expressed as (Mignone et al., 2007a):

$$\frac{\partial E}{\partial t} + \nabla \cdot \left(\mathbf{F}^{\rm adv} - \kappa \nabla T \right) = 0 \,, \tag{2.30}$$

Here, $\mathbf{F}^{adv}$ represents the energy advection flux while κ depicts the coefficient of thermal conduction. With the additional time step constraint, these parabolic terms can be included into the original energy equation representing a conservation law. The $\Delta t = \min(\Delta t^{\rm ad}, \Delta t^{\rm par})$, where $\Delta t^{\rm ad}$ depicts the advective time step (Eq. 2.25), which incorporates in the PLUTO as (Mignone et al., 2007a):

$$\Delta t^{\rm par} < 0.5 \min_{d=1,2,3} \left[\frac{\left(\Delta x^d\right)^2}{\max(\sigma)} \right]. \tag{2.31}$$

Here σ may be the resistivity coefficient (η) or thermal conductivity coefficient (κ).

In case of simulations with increasing resolution and diffusion-dominated problems, $\Delta t^{\rm par}$ can fall below a certain advection scale. In these cases, the super time stepping (STS) approach (already incorporate in PLUTO) can significantly speed up the explicit integration (see Alexiades et al., 1996; O'Sullivan and Downes, 2007). STS incorporates heat diffusion terms through operator splitting. Thereafter, the solution vector evolves across a super time step ΔT containing N smaller sub-steps. It can be expressed as:

$$\Delta T \rightarrow N^2 \Delta t^{\rm par}, \tag{2.32}$$

Therefore, STS is approximately N times faster compared to the standard explicit approach.

2.4.9 Units and dimensions

The PLUTO code compute the set of MHD equations by using the normalization (dimensionless) of all the variables by three parameters i.e., UNIT_LENGTH (L_0), UNIT_DENSITY (ρ_0) and UNIT_VELOCITY (V_0) (Mignone et al., 2007a). The L_0, ρ_0, and V_0 are utilized to construct new dimensionless parameters, which are then substituted back into the MHD PDEs. These methods will be intact but now include an operator for all the used variables rather than the variable themselves. These normalization of the physical variables do not affect the MHD equations by the size of the plasma, strength of the magnetic field, time, density, etc. In our present simulation, we adopt the values of $L_0 = 10^8$ cm, $\rho_0 = 10^{-15} gcm^{-3}$, and $V_0 = 10^8\ cms^{-1}$. These values are corresponding to the observational data in the solar atmosphere at height (reference level) y=10 Mm in its corona.

Furthermore, the unit of time is estimated by $t_0 = L_0/V_0$, the unit of pressure ($p_0 = \rho_0 V_0^2$), and unit of strength of the magnetic field is expressed as $B_0 = \sqrt{4\pi\rho_0 V_0^2}$. Therefore, we can convert the normalized values in the CGS unit system in terms of these factors of

L_0, ρ_0, V_0, p_0, and B_0, etc as follows (Mignone et al., 2007a):

$$\rho = \frac{\rho_{cgs}}{\rho_0}, V = \frac{V_{cgs}}{V_0}, p = \frac{p_{cgs}}{\rho_0 V_0^2}, B = \frac{B_{cgs}}{\sqrt{4\pi\rho_0 V_0^2}} \tag{2.33}$$

Apart from above mentioned simulation method, the set of MHD PDEs are solved using the PLUTO code with the implementation of initial conditions such as grid domain and resolutions, time step, temporal resolution, values of physical variables, expressions for the specific conditions, etc which are described in detailed in the associated chapters (Chapters 3, 4, 5, and 6). We also set the time-dependent physical conditions (such as non-ideal parameters, equation of state, etc), as well as other regulating factors. In addition, the boundary conditions for individual problems are examined in detail in the preceding chapters.

2.5 Wavelet Analysis Technique

Wavelet analysis [5] is a technique that is used to examine the quasi-periodic signals in real observational domain or numerical simulation domain.A Fourier transform is required which identifies the dominant frequencies present in the quasi-periodic signals. Wavelet analysis, which is based on the wavelet transform, has an advantage of giving temporal localization of the various frequency components. Therefore, it makes possible to examine both the frequency (or period) and the real time information of any Fourier periods contained in the data (Torrence and Compo, 1998). Torrence and Compo (1998) proposed the wavelet transform which is a function of time series (i.e., X_N, where N is the no. of observations), sample spacing (i.e., δt). Therefore, Wavelet transform is termed as the convolution of X_N with a scaled mother function ψ_η, where, η is the non-dimensional parameter. The chosen wavelet functions is localised with zero mean in both time and

[5]https://paos.colorado.edu/research/wavelets/

Fourier period (or frequency) space, therefore we presume they are normalised. Therefore, the continuous wavelet transform is given as (e.g., Torrence and Compo, 1998):

$$\int_{-\infty}^{\infty} \psi\psi^* d\eta = 1 \tag{2.34}$$

The Wavelet transform is expressed as (Torrence and Compo, 1998):

$$W_x(s) = \sum_{k=0}^{N-1} x_{n'} \sqrt{\frac{\delta x}{s}} \psi^*[\frac{(n'-n)\delta t}{s}], \tag{2.35}$$

where, $W_x(s)$ is the wavelet power spectrum. The $\frac{(n'-n)\delta t}{s} = \eta$ is the scale of the wavelet.The wavelet function will be translated w.r.t time is represented by the letter "n". Therefore, a 2D power spectrum (cf., Chapter 3 for example) is produced by changing the wavelet scales and translating it along the time index n. This depicts the variation in period as a function of the time and scale. The edge effects at the endpoints of the time series occurred, however, they are caused by the wavelet finiteness function and are proportional to the chosen scale. This means that a cone of influence (COI) is the region where wavelet strength decreases by a factor of 'e' and edge effects are difficult to ignore. The edge effects cause the wavelet power spectrum outside COI thus excluded from our study. The significance level in the wavelet power spectrum of any periods is a factor that examine the quality of the wavelet analysis. The expected background noise spectrum is compared to the data power spectrum. Within certain significance contours, wavelet power is deemed to be real at a particular degree of the confidence level. We use the red-noise and, power law estimations to compute the significance levels of the wavelet analysis that we performed on the time-varying signals of mass fluxes derived from the simulations in Chapter 3. Some details of the wavelet analysis are also described in Chapter 3.

In conclusion, this Chapter has provided the focused overview of the utilized observational data from various observatories and their onboard instruments, as well as analysis

techniques. It also described the numerical simulation methods of PLUTO as developed by Mignone et al. (2007a) that are utilized in the present thesis. In the next Chapter, we discuss the scientific results related to the numerical model of the Alfvén pulse driven quasi-periodic spicule-like cool jets.